Inorg. Chem. **2007**, *46*, 384–394

Assignment of Molecular Structures to the Electrochemical Reduction Products of Diiron Compounds Related to [Fe–Fe] Hydrogenase: A Combined Experimental and Density Functional Theory Study

Stacey J. Borg,[†] Jesse W. Tye,[‡] Michael B. Hall,*[,‡] and Stephen P. Best*[,†]

School of Chemistry, University of Melbourne, 3010 Victoria, Australia, and Department of Chemistry, Texas A&M University, College Station, Texas 77843-3255

Received July 2, 2006

The reduction chemistry of (μ-bridge)[Fe(CO)$_3$]$_2$ [bridge = propane-1,3-dithiolate (**1**) and ethane-1,2-dithiolate (**2**)] is punctuated by the formation of distinct products, resulting in a marked difference in CO inhibition of electrocatalytic proton reduction. The products formed following reduction of **2** have been examined by a range of electrochemical, spectroelectrochemical, and spectroscopic approaches. Density functional theory has allowed assessment of the relative energies of the structures proposed for the reduction products and agreement between the calculated spectra (IR and NMR) and bond distances with the experimental spectra and EXAFS-derived structural parameters. For **1** and **2**, one-electron reduction is accompanied by dimerization, but the structure, stability, and reaction with CO of the dimer is different in the two cases, and this is responsible for the different CO inhibition response for electrocatalytic proton reduction. Calculations of the alternate structures of the two-electron, one-proton reduced forms of **2** show that the isomers with terminally bound hydrides are unlikely to play a significant role in the chemistry of these species. The hydride-transfer chemistry of the **1B** species is more reasonably attributed to a hydride-bridged form. The combination of experimental and computational results provides a solid foundation for the interpretation of the reduction chemistry of dithiolate-bridged diiron compounds, and this will underpin translation of the diiron subsite of the [FeFe] hydrogenase H cluster into an abiological context.

Introduction

The potential of dihydrogen (H_2) to be the dominant energy carrier in the transition from the hydrocarbon-based technologies hinges on the development of simple and efficient methods of its production and utilization. A key piece in this puzzle is the development of a low-cost high-abundance replacement for Pt as the H_2 activation catalyst suitable for efficient operation of low-temperature fuel cells. In nature, proton reduction and H_2 oxidation are readily accomplished by the base metal-containing hydrogenase (H_2ase) enzymes. Protein crystallography has revealed that the active sites of these enzymes are composed of dinuclear Fe−Fe or Ni−Fe centers bridged by thiolate S atoms (as shown in Figure 1).[1] It has been shown that H_2ase-modified graphite electrodes are capable of producing and utilizing H_2 at electrochemical potentials and with catalytic efficiencies that rival those of Pt-based electrodes.[2]

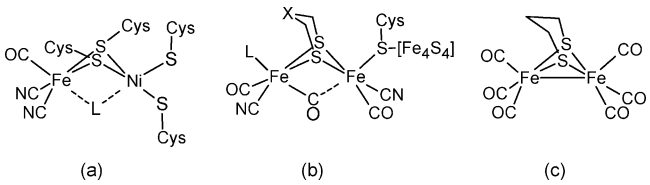

Figure 1. Representations of the active site structures of the crystallographically characterized (a) [NiFe]- and (b) [FeFe]H_2ases together with the structure of **1**, (μ-pdt)[Fe(CO)$_3$]$_2$ (c).

The molecular structures of the H_2ase enzyme active sites provide blueprints for the design of new base−metal electrocatalysts for proton reduction and H_2 oxidation. Although the Ni−Fe hydrogenase ([NiFe]H_2ase) enzymes are generally considered to be more robust and have been extensively studied,[3] the Fe−Fe hydrogenase ([FeFe]H_2ase) active site has been the subject of more synthetic model studies because of the similarity of the active site to previously known complexes of the form (μ-SRS)[Fe(CO)$_3$]$_2$.[4]

The ability of small-molecule analogues of the [FeFe]H_2ase active site to catalyze proton reduction is now well documented.[5−10] The [Et$_4$N$^+$]$_2$[(μ-pdt)[Fe(CO)$_2$(CN)]$_2$] (pdt = propane-1,3-dithiolate) complex reacts with triflic acid

* To whom correspondence should be addressed. E-mail: mbhall@tamu.edu (M.B.H.), spbest@unimelb.edu.au (S.P.B.).
[†] University of Melbourne.
[‡] Texas A&M University.

10.1021/ic061211t CCC: $37.00
Published on Web 10/13/2006

(HOTf) to yield substoichiometric amounts of H_2 (~35% yield based on the diiron compound) and an oxidized, insoluble material[11] but does not function as a solution electrocatalyst for H_2 production in H_2O in the pH range from 8.4 to 4.0.[12] In terms of the overpotential required to affect H_2 production, the best diiron model system to date is the mixed ligand complex $[(\mu\text{-pdt})[Fe(CO)_2(CN)][Fe(CO)_2(PMe_3)]]^-$, which produces H_2 at −1.13 V vs Ag/AgCl from CH_3CN solutions of strong acids, such as H_2SO_4.[13] Higher nuclearity Fe compounds involving either a diiron center linked to a 4Fe4S cluster or a tetrairon compound formed from dimerization of diiron units operate, albeit slowly, at somewhat more positive potentials.[9,10]

Although more precise structural models and better functional models have been made, the simple hexacarbonyl complexes (μ-pdt)[Fe(CO)$_3$]$_2$ (**1**) and (μ-edt)[Fe(CO)$_3$]$_2$ (**2**; edt = ethane-1,2-dithiolate) share a common topology with the active site of the [FeFe]H$_2$ase enzymes (Figure 1) and electrocatalyze proton reduction. A detailed examination of electrocatalytic proton reduction by **1** has recently been published.[8]

While having a similar {2Fe2S} core geometry, the reduction chemistry of **1** and **2** may be markedly different; for example, electrocatalytic proton reduction is strongly inhibited by CO for **1**, but no change in electrocatalysis by CO is apparent for **2**.[14] Because CO contamination is a problem for H_2 produced by water-gas shift reactions, the difference in CO inhibition is of great practical importance for H activation catalysts based on this chemistry. An important driver for this study is the rationalization of the different catalytic behavior of **1** and **2**, and this requires the delineation of the reduction products formed following reduction. More generally, it is our belief that a detailed understanding of the electrochemistry of these simple diiron dithiolate complexes underpins the rational design of more efficient and more robust biomimetic electrocatalysts based on [FeFe]H$_2$ase.

This Article details chemical, electrochemical, spectroscopic, and theoretical (density functional theory, DFT) examinations of complex **2**. An understanding of the chemical and structural changes that follow the reduction of these complexes is developed through comparison of the experimentally determined IR and NMR spectra of the electrogenerated species with DFT-derived predicted spectra of the various structural candidates.

Experimental Section

General Procedures. Samples of (μ-pdt)[Fe(CO)$_3$]$_2$ (**1**) and (μ-edt)[Fe(CO)$_3$]$_2$ (**2**) were prepared by literature methods[15] and confirmed to be pure by spectroscopic and electrochemical analyses. Solvents were purified and dried using standard methods[16] and were distilled under an atmosphere of N_2 immediately prior to use. Solutions used for electrochemical or spectroscopic analyses were prepared under an atmosphere of N_2 or Ar either using standard Schlenk techniques or with the aid of a Vacuum Atmospheres glovebox. High-purity Ar, N_2, and CO gases were obtained from BOC gases. Tetra-*n*-butylammonium perchlorate (TBA[ClO_4]) and tetra-*n*-butylammonium hexafluorophosphate (TBA[PF_6]), used as supporting electrolytes, were prepared and purified using standard procedures.[17] ***Caution!*** *Perchlorate salts are potentially explosive. Solutions containing TBA[ClO_4] as a supporting electrolyte should not be allowed to evaporate to dryness.*

Solutions of $[(\mu\text{-edt})[Fe_2(CO)_5(HCO)]]^-$ were prepared by mixing equimolar solutions of **2** and Li[$BH(Et)_3$] in tetrahydrofuran (THF). Solution flow through narrow-bore (0.5-mm-i.d.) Teflon tubing was controlled using syringe pumps.

(1) Volbeda, A.; Charon, M.-H.; Piras, C.; Hatchikian, E. C.; Frey, M.; Fontecilla-Camps, J. C. *Nature* **1995**, *373*, 580−587. Volbeda, A.; Garcin, E.; Piras, C.; de Lacey, A. L.; Fernández, V. M.; Hatchikian, E. C.; Frey, M.; Fontecilla-Camps, J. C. *J. Am. Chem. Soc.* **1996**, *118*, 12989−12996. Nicolet, Y.; Lemon, B. J.; Fontecilla-Camps, J. C.; Peters, J. W. *Trends Biochem. Sci.* **2000**, *25*, 138−143. Peters, J. W.; Lanzilotta, W. N.; Lemon, B. J.; Seefeldt, L. C. *Science* **1998**, *282*, 1853−1858. Lemon, B. J.; Peters, J. W. *Biochemistry* **1999**, *38*, 12969−12973. Nicolet, Y.; Piras, C.; Legrand, P.; Hatchikian, C. E.; Fontecilla-Camps, J. C. *Structure* **1999**, *7*, 13−23. Nicolet, Y.; de Lacey, A. L.; Vernede, X.; Fernandez, V. M.; Hatchikian, E. C.; Fontecilla-Camps, J. C. *J. Am. Chem. Soc.* **2001**, *123*, 1596−1601. Volbeda, A.; Montet, Y.; Vernede, X.; Hatchikian, E. C.; Fontecilla-Camps, J. C. *Int. J. Hydrogen Energy* **2002**, *27*, 1449−1461.

(2) Krasna, A. I.; Rittenberg, D. *J. Am. Chem. Soc.* **1954**, *76*, 3015−3020. Butt, J. N.; Filipiak, M.; Hagen, W. R. *Eur. J. Biochem.* **1997**, *245*, 116−122. Adams, M. W. W. *Biochim. Biophys. Acta* **1990**, *1020*, 115−145.

(3) Frey, M. *Struct. Bonding* **1998**, *90*, 98−126. Volbeda, A.; Fontecilla-Camps, J. C. *Coord. Chem. Rev.* **2005**, *249*, 1609−1619. de Lacey, A. L.; Fernandez, V. M.; Rousset, M. *Coord. Chem. Rev.* **2005**, *249*, 1596−1608. Frey, M. *ChemBioChem* **2002**, *3*, 153−160.

(4) Reihlen, H.; Gruhl, A.; van Hessling, G. *Ann.* **1929**, *472*, 268−287. Hieber, W.; Spacu, P. *Z. Anorg. Allg. Chem.* **1937**, *233*, 353−364. Fauvel, K.; Mathieu, R.; Poilblanc, R. *Inorg. Chem.* **1976**, *15*, 976−978. Seyferth, D.; Henderson, R. S.; Song, L. C. *Organometallics* **1982**, *1*, 125−133. Winter, A.; Zsolnai, L.; Huttner, G. *Z. Naturforsch., B: Chem. Sci.* **1982**, *37B*, 1430−1436. Treichel, P. M.; Rublein, E. K. *J. Organomet. Chem.* **1989**, *359*, 195−203. Seyferth, D.; Womack, G. B.; Gallagher, M. K.; Cowie, M.; Hames, B. W.; Fackler, J. P., Jr.; Mazany, A. M. *Organometallics* **1987**, *6*, 283−294.

(5) Gloaguen, F.; Lawrence, J. D.; Rauchfuss, T. B.; Bénard, M.; Rohmer, M.-M. *Inorg. Chem.* **2002**, *41*, 6573−6582. Mejia-Rodriguez, R.; Chong, D.; Reibenspies, J. H.; Soriaga, M. P.; Darensbourg, M. Y. *J. Am. Chem. Soc.* **2004**, *126*, 12004−12014. Ott, S.; Kritikos, M.; Åkermark, B.; Sun, L.; Lomoth, R. *Angew. Chem., Int. Ed.* **2004**, *43*, 1006−1009. Capon, J.-F.; Gloaguen, F.; Schollhammer, P.; Talarmin, J. *J. Electroanal. Chem.* **2004**, *566*, 241−247. Li, P.; Wang, M.; He, C.; Li, G.; Liu, X.; Chen, C.; Akermark, B.; Sun, L. *Eur. J. Inorg. Chem.* **2005**, 2506−2513. Borg, S. J.; Bondin, M. I.; Best, S. P.; Razavet, M.; Liu, X.; Pickett, C. J. *Biochem. Soc. Trans.* **2005**, *33*, 3−6. Liu, T.; Wang, M.; Shi, Z.; Cui, H.; Dong, W.; Chen, J.; Akermark, B.; Sun, L. *Chem.−Eur. J.* **2004**, *10*, 4474−4479.

(6) Chong, D.; Georgakaki, I. P.; Mejia-Rodriguez, R.; Sanabria-Chinchilla, J.; Soriaga, M. P.; Darensbourg, M. Y. *Dalton Trans.* **2003**, 4158−4163.

(7) Cheah, M. H.; Borg, S. J.; Bondin, M. I.; Best, S. P. *Inorg. Chem.* **2004**, *43*, 5635−5644.

(8) Borg, S. J.; Behrsing, T.; Best, S. P.; Razavet, M.; Liu, X.; Pickett, C. J. *J. Am. Chem. Soc.* **2004**, *126*, 16988−16999.

(9) Tard, C.; Liu, X.; Hughes, D. L.; Pickett, C. J. *Chem. Commun.* **2005**, 133−135.

(10) Tard, C.; Liu, X.; Ibrahim Saad, K.; Bruschi, M.; De Gioia, L.; Davies, S. C.; Yang, X.; Wang, L.-S.; Sawers, G.; Pickett, C. J. *Nature* **2005**, *433*, 610−613.

(11) Schmidt, M.; Contakes, S. M.; Rauchfuss, T. B. *J. Am. Chem. Soc.* **1999**, *121*, 9736−9737.

(12) Cloirec, A. L.; Davies, S. C.; Evans, D. J.; Hughes, D. L.; Pickett, C. J.; Best, S. P.; Borg, S. *Chem. Commun.* **1999**, 2285−2286.

(13) Gloaguen, F.; Lawrence, J. D.; Rauchfuss, T. B. *J. Am. Chem. Soc.* **2001**, *123*, 9476−9477.

(14) Borg, S. J. Redox interconversion chemistry of diiron carbonyl complexes. Ph.D. Thesis, The University of Melbourne, Melbourne, Australia, 2005.

(15) Lyon, E. J.; Georgakaki, I. P.; Reibenspies, J. H.; Darensbourg, M. Y. *J. Am. Chem. Soc.* **2001**, *123*, 3268−3278.

(16) Errington, R. J. *Guide to Practical Inorganic and Organo-Metallic Chemistry*; Blackie Academic & Professional: London, 1997.

(17) Sawyer, D. T.; Sobkowiak, A.; Roberts, J. J. L. *Electrochemistry for Chemists*, 2nd ed.; Wiley-Interscience: New York, 1995.

Spectroelectrochemistry (SEC). A PAR model 362 scanning potentiostat was used for the SEC experiments, and these were conducted using a purpose-built reflection/absorption cell capable of operating at moderate gas pressures (1 MPa). The design and operation of the high-pressure SEC cell have previously been described.[18] The current response of the SEC cell was monitored using a Powerlab 4/20 interface and Chart 4 software (ADInstruments). The potential of the reference electrode was determined using the ferrocenium/ferrocene (Fc^+/Fc) couple, and all potentials are quoted relative to the SCE reference electrode. Against this reference, the Fc^+/Fc couple occurs at +0.38 V in CH_3CN and at +0.53 V in THF.[19] The solution under spectroscopic interrogation was comprised of a 10−30-μm layer of solution trapped between the 3-mm-diameter working electrode and a CaF_2 window. The thickness of the layer was adjusted under micrometer control and its value estimated using the extinction coefficients of absorptions due to the solvent.[20]

The IR−SEC spectra were collected in single-beam mode, and differential absorbance spectra were calculated from these using the spectrum recorded immediately prior to the application of the potential step as the reference. Spectra for the individual reduced species were obtained by spectral subtraction using Grams/32 AI software (Galactic). In cases where the band profiles of the component species were overlapping, their relative concentrations were obtained by multicomponent analysis using routines available within the Igor Pro program (Wavemetrics).

Continuous-flow electrosynthesis experiments were carried out using a purpose-built cell that incorporates a reticulated C working electrode. The design of the cell has previously been reported.[21]

EXAFS Sample Preparation and Analysis. Fe K-edge (7112-eV) X-ray absorption measurements were conducted using the bending magnet source of beamline 20B at the KEK Photon Factory, Tsukuba, Japan. Monochromatic radiation was provided by a channel-cut Si(111) monochromator with an energy resolution ($\Delta E/E$) of ca. 2.4×10^{-4}, where higher order harmonics were rejected by detuning the monochromator so as to reduce the beam intensity to approximately half of its maximum value. Solutions were measured in fluorescence mode using a 10-element Ge detector (Canberra). Data analysis was conducted using the *Xfit* suite of programs,[22] which incorporates *FEFF* version 6.01.[23] Details of the procedures followed for the analysis or related systems have been described previously.[7,8,24] Samples of the reduced compounds were generated by continuous-flow electrosynthesis[21] using 5 mM (i.e., 10 mM in Fe) solutions of **2** in CH_3CN/0.2 M TBA[PF_6]. The composition of the solution was monitored, in line, by IR spectroscopy (Shimadzu, Prestige) and the sample freeze-quenched in either liquid N_2 or isopentane (−130 °C).

Instrumentation. IR−SEC experiments were conducted using a Biorad FT175C FTIR spectrometer utilizing a Ge/KBr beam splitter and a narrow-band MCT detector. A Bruker ECS 106 X-band spectrometer was used to collect electron paramagnetic resonance (EPR) spectra, and a Varian Unity Plus 400 MHz instrument was used to record the NMR spectra.

Computational Details

All DFT calculations were performed using a hybrid functional [the three-parameter exchange functional of Becke (B3) and the correlation functional of Lee, Yang, and Parr (LYP), B3LYP],[25] as implemented in *Gaussian 03*.[26] The Fe, P, and S atoms use the effective core potential and associated basis set of Hay and Wadt (LANL2DZ).[27] For Fe, the two outermost p functions were replaced by reoptimized 4p functions, as suggested by Couty and Hall.[28] For S and P, the basis set was augmented by the d polarization function of Höllwarth et al.[29] The carbon and hydrogen atoms of the μ-SCH_2CH_2S and μ-$SCH_2CH_2CH_2S$ linkers use Dunning's double-ζ basis (D95) and all other atoms use Dunning's correlation-consistent polarized valence double-ζ basis set (cc-pVDZ).[30] Unless otherwise noted, all geometries are fully optimized and confirmed as minima or *n*-order saddle points by analytical frequency calculations at the same level of theory. The computed ν(CO) values were scaled using a multiplicative factor of 0.9641; this scaling factor gives the best agreement between the gas-phase-computed and experimentally determined IR spectra for the three complexes (μ-$S(CH_2)_2S$)[$Fe(CO)_3$]$_2$, (μ-$S(CH_2)_3S$)[$Fe(CO)_3$]$_2$, and (μ-$SCH_2(C_6H_4)CH_2S$)[$Fe(CO)_3$]$_2$. The calculated ν(CO) spectra presented in the paper are based on gas-phase species and are simulated using Gaussian functions with a full width at half-height (fwhh) of 10 cm^{-1}.

Solvation calculations employing CH_3CN and THF solvents were performed on the fully optimized gas-phase geometries using the Polarizable Continuum Model[31] with the scrf=(pcm,solvent=CH3CN) and scrf=(pcm,solvent=THF) keywords as implemented in *Gaussian 03*.

(18) Borg, S. J.; Best, S. P. *J. Electroanal. Chem.* **2002**, *535*, 57−64.
(19) Chang, D.; Malinski, T.; Ulman, A.; Kadish, K. M. *Inorg. Chem.* **1984**, *23*, 817−824. Connelly, N. G.; Geiger, W. E. *Chem. Rev.* **1996**, *96*, 877−910.
(20) Goplen, T. G.; Cameron, D. G.; Jones, R. N. *Appl. Spectrosc.* **1980**, *34*, 657−691. Christensen, P. A.; Hamnett, A.; Higgins, S. J.; Timney, J. A. *J. Electroanal. Chem.* **1995**, *395*, 195−209.
(21) Bondin, M. I.; Foran, G.; Best, S. P. *Aust. J. Chem.* **2001**, *54*, 705−709.
(22) Ellis, P. J. *Xfit for Windows 95*; Australian Synchrotron Research Program: Sydney, Australia, 1996. Ellis, P. J.; Freeman, H. C. *J. Synchrotron Radiat.* **1995**, *2*, 190−195.
(23) Zabinsky, S. I.; Rehr, J. J.; Ankudinov, A.; Albers, R. C.; Eller, M. J. *Phys. Rev. B: Condens. Matter Phys.* **1995**, *52*, 2995−3009.
(24) Bondin, M. I.; Borg, S. J.; Cheah, M. H.; Foran, G.; Best, S. P. *Aust. J. Chem.* **2006**, *59*, 263−272.
(25) Becke, A. D. *J. Chem. Phys.* **1993**, *98*, 5648−5652. Lee, C.; Yang, W.; Parr, R. G. *Phys. Rev. B: Condens. Matter* **1988**, *37*, 785−789.
(26) Frisch, M. J.; Trucks, G. W.; Schlegel, H. B.; Scuseria, G. E.; Robb, M. A.; Cheeseman, J. R.; Montgomery, J. A., Jr.; Vreven, T.; Kudin, K. N.; Burant, J. C.; Millam, J. M.; Iyengar, S. S.; Tomasi, J.; Barone, V.; Mennucci, B.; Cossi, M.; Scalmani, G.; Rega, N.; Petersson, G. A.; Nakatsuji, H.; Hada, M.; Ehara, M.; Toyota, K.; Fukuda, R.; Hasegawa, J.; Ishida, M.; Nakajima, T.; Honda, Y.; Kitao, O.; Nakai, H.; Klene, M.; Li, X.; Knox, J. E.; Hratchian, H. P.; Cross, J. B.; Bakken, V.; Adamo, C.; Jaramillo, J.; Gomperts, R.; Stratmann, R. E.; Yazyev, O.; Austin, A. J.; Cammi, R.; Pomelli, C.; Ochterski, J. W.; Ayala, P. Y.; Morokuma, K.; Voth, G. A.; Salvador, P.; Dannenberg, J. J.; Zakrzewski, V. G.; Dapprich, S.; Daniels, A. D.; Strain, M. C.; Farkas, O.; Malick, D. K.; Rabuck, A. D.; Raghavachari, K.; Foresman, J. B.; Ortiz, J. V.; Cui, Q.; Baboul, A. G.; Clifford, S.; Cioslowski, J.; Stefanov, B. B.; Liu, G.; Liashenko, A.; Piskorz, P.; Komaromi, I.; Martin, R. L.; Fox, D. J.; Keith, T.; Al-Laham, M. A.; Peng, C. Y.; Nanayakkara, A.; Challacombe, M.; Gill, P. M. W.; Johnson, B.; Chen, W.; Wong, M. W.; Gonzalez, C.; Pople, J. A. *Gaussian 03*, revision B.05; Gaussian, Inc.: Wallingford, CT, 2004.
(27) Hay, P. J.; Wadt, W. R. *J. Chem. Phys.* **1985**, *82*, 270−283. Hay, P. J.; Wadt, W. R. *J. Chem. Phys.* **1985**, *82*, 284−298.
(28) Couty, M.; Hall, M. B. *J. Comput. Chem.* **1996**, *17*, 1359−1370.
(29) Höllwarth, A.; Böhme, M.; Dapprich, S.; Ehlers, A. W.; Gobbi, A.; Jonas, V.; Köhler, K. F.; Stegmann, R.; Veldkamp, A.; et al. *Chem. Phys. Lett.* **1993**, *208*, 237−240.
(30) Dunning, T. H., Jr.; Hay, P. J. In *Methods of Electronic Structure Theory*; Schaefer, H. F., III, Ed.; Plenum Press: New York, 1977; Vol. 3. Dunning, T. H., Jr. *J. Chem. Phys.* **1970**, *53*, 2823−2833. Dunning, T. H., Jr. *J. Chem. Phys.* **1989**, *90*, 1007−1023.

NMR shielding tensors are calculated using the Gauge-Independent Atomic Orbital (GIAO) method as implemented in *Gaussian 03*.[32] The basis sets and level of theory used in the NMR calculations are the same as those described above. The NMR calculation yields values of the NMR shielding tensor for a given atom in a given molecule. The chemical shift of a particular H atom versus tetramethylsilane (TMS), δ, is the difference in the NMR shielding tensor of the H atom in the molecule of interest, σ, and the NMR shielding tensor for the H atoms in TMS, σ_{TMS} (i.e., $\delta = \sigma - \sigma_{TMS}$). The chemical shift values reported in this Article are determined by using the value of σ_{TMS} determined by setting the computed value for the chemical shift of the hydride ligand of $[HFe(CO)_4]^-$ equal to the experimentally observed chemical shift for the compound in THF (−8.81 ppm relative to TMS).[33] This method should yield a more accurate value of the chemical shift than direct computation of σ_{TMS} because of a greater cancellation of error, and it is shown to faithfully reproduce the experimentally determined chemical shifts for the hydride ligands in *cis*-$(H)_2Fe(CO)_4$, $[(\mu^3\text{-}S)(\mu^2\text{-}H)[Fe(CO)_3]_3]^-$, and $(\mu^3\text{-}S)(\mu^2\text{-}H)_2[Fe(CO)_3]_3$.[33,34]

Results and Discussion

The techniques described herein have enabled the identification of a number of transient IR spectra that can be attributed to individual species formed by various chemical and electrochemical reactions. These species are systematically designated as an alpha−numeric label (e.g., **1A**). The number identifies the parent complex [e.g., (μ-pdt)[Fe(CO)$_3$]$_2$ (**1**) and (μ-edt)[Fe(CO)$_3$]$_2$ (**2**)], while the letter relates to a unique IR spectral signature. For example, although species **1A** and **2A** are derived from different parent complexes, they have nearly indistinguishable IR spectra in the ν(CO) region, and therefore presumably similar structures. A collection of the IR spectra of various species derived from **1** and **2**, together with the structures previously suggested[8] for **1A**, **1B**, and **1C**, are shown in Figure 2. DFT-calculated species are enclosed in square brackets (e.g., **[2(a)]**$^-$).

The electrochemistry of **1** and **2** has previously been reported.[6] Two irreversible reduction waves were observed with E_{pc} values of ca. −1.3 and −1.9 V (vs SCE), which have been attributed to successive one-electron reductions. In common with related compounds, an improvement in the reversibility of the first reduction is obtained for solutions saturated with CO.[35] Whereas the primary reduction waves of compounds **1** and **2** are one-electron process, the irreversible behavior is associated with the formation of products related to the starting material by net two-electron transfer.[8]

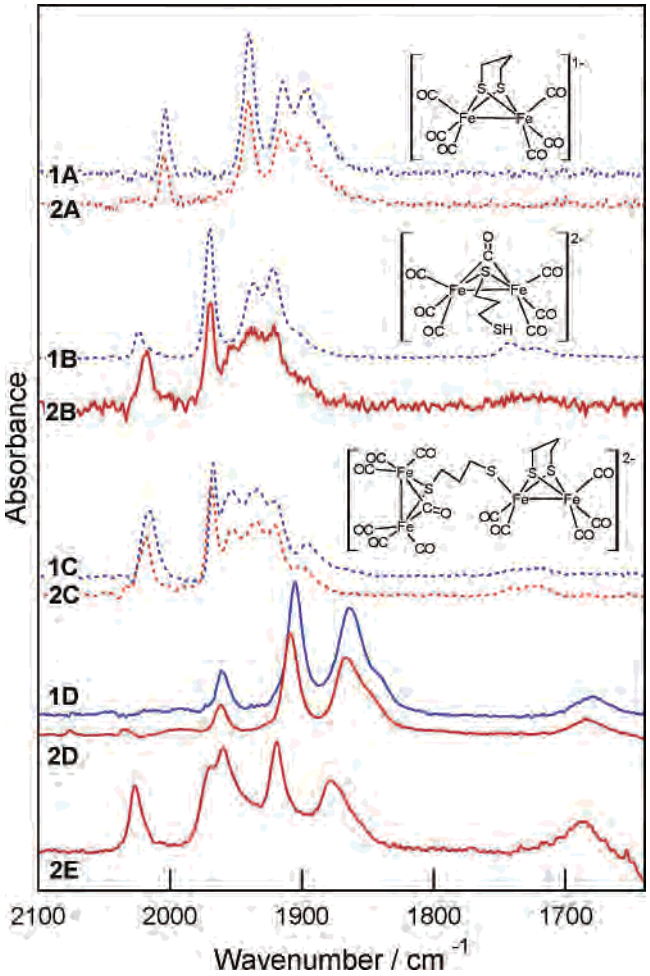

Figure 2. IR spectra of individual species as isolated from SEC or continuous-flow electrosynthesis experiments. The spectra were obtained using either CH_3CN (solid line) or THF (dotted line) as the solvent, with TBA[ClO_4] as the supporting electrolyte. The spectrum of **2B** is weak and is contaminated with **2C**. The structures shown for the **1A**, **1B**, and **1C** species are based on those proposed in ref 8.

SEC of 2

Reduction of **2** in CH_3CN under an inert atmosphere at mild potentials (−1.2 V) results in a complicated spectral profile including at least nine ν(CO) bands (Figure 3a). The product spectrum is simplified by application of a more strongly reducing potential (Figure 3b), with the four-band ν(CO) spectrum attributed to a single product designated as **2D** (Figure 2). Reoxidation at mild potentials (−0.9 V) results in the rapid loss of **2D** and concomitant recovery of **2** together with a set of ν(CO) bands at 2027, 1969, 1961, 1940, 1919, 1879, and 1690 cm^{-1} (Figure 3c). On the basis of the observation that the relative intensities of the component bands remain constant during the SEC experiments, the seven ν(CO) band profile is attributed to a single species, **2E**.

(31) Cammi, R.; Mennucci, B.; Tomasi, J. *J. Phys. Chem. A* **2000**, *104*, 5631−5637. Cammi, R.; Mennucci, B.; Tomasi, J. *J. Phys. Chem. A* **1999**, *103*, 9100−9108. Mennucci, B.; Cances, E.; Tomasi, J. *J. Phys. Chem. B* **1997**, *101*, 10506−10517. Mennucci, B.; Tomasi, J. *J. Chem. Phys.* **1997**, *106*, 5151−5158.

(32) London, F. *J. Phys. Radium* **1937**, *8*, 397−409. Ditchfield, R. *Mol. Phys.* **1974**, *27*, 789−807. Wolinski, K.; Hinton, J. F.; Pulay, P. *J. Am. Chem. Soc.* **1990**, *112*, 8251−8260. Ruud, K.; Helgaker, T.; Bak, K. L.; Jørgensen, P.; Jensen, H. J. A. *J. Chem. Phys.* **1993**, *99*, 3847−3859.

(33) Krusic, P. J.; Jones, D. J.; Roe, D. C. *Organometallics* **1986**, *5*, 456−460.

(34) Marko, L.; Takacs, J.; Papp, S.; Marko-Monostory, B. *Inorg. Chim. Acta* **1980**, *45*, L189−L90. van Hal, J. W.; Whitmire, K. H. *Organometallics* **1998**, *17*, 5197−5201. Cherng, J.-J.; Tsai, Y.-C.; Ueng, C.-H.; Lee, G.-H.; Peng, S.-M.; Shieh, M. *Organometallics* **1998**, *17*, 255−261.

(35) Darchen, A.; Mousser, H.; Patin, H. *J. Chem. Soc., Chem. Commun.* **1988**, 968−970.

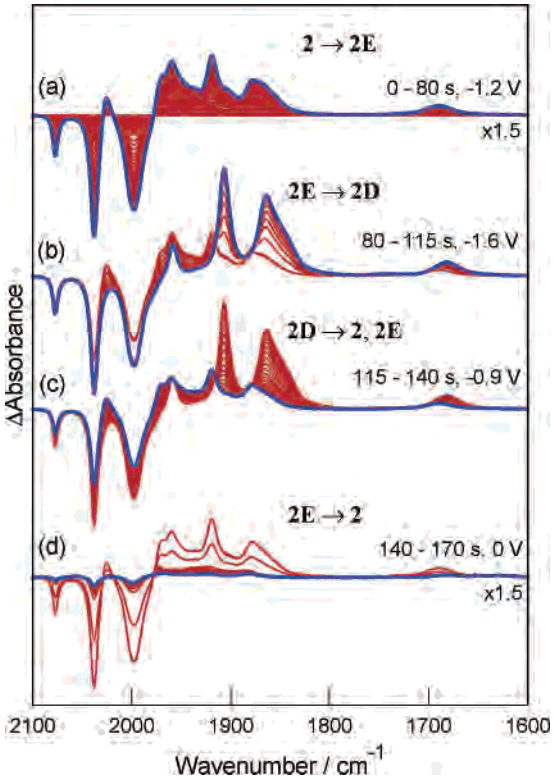

Figure 3. Differential absorbance IR spectra recorded following the reduction and reoxidation of a 1 mM CH_3CN solution of **2** under an inert atmosphere (0.1 M TBA[ClO_4], 275 kPa Ar). The bold lines indicate the last spectrum in the set. The applied potentials, times, and predominant chemical transformations are shown for each set of spectra.

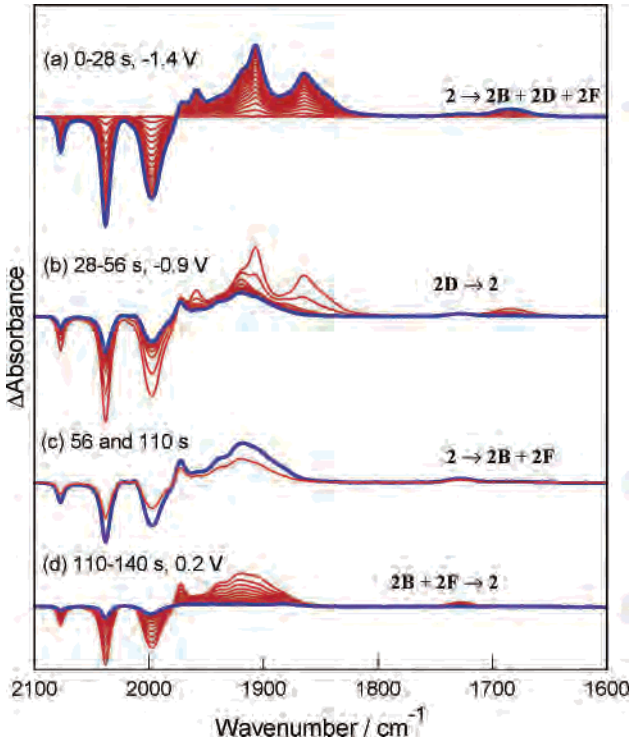

Figure 4. Differential absorption IR spectra obtained during the reduction and reoxidation of a 1 mM CH_3CN solution of **2** under CO (0.2 M TBA-[ClO_4], 275 kPa CO). The spectra shown in part c are recorded at an applied potential of −0.9 V initially (56 s) and then the potential is switched to between −1.4 and −0.9 V (110 s). The bold lines indicate the last spectrum in each set.

Reduction at mild potentials results in predominant formation of **2E**, with the formation of **2D** increasingly important at more reducing potentials. The net transfer of two electrons to **2** during the formation of **2D** has been confirmed by quantification of the charge transferred into the thin layer using the approach described in an earlier report.[8] These experiments, conducted under an atmosphere of CO, show that the conversion of **2** to **2D** requires two electrons (1.8 ± 0.2). Mild oxidation results in the conversion of **2D** into **2E**, and application of a more strongly oxidizing potential results in near-quantitative recovery of the starting material (Figure 3d). The first observable reduction product in the IR spectra, **2E**, clearly has a redox level intermediate between that of **2** and **2D**. The observation of a seven ν(CO) band profile for **2E** requires that this species either be present as a dimer or be a monomeric species in rapid equilibrium with an isomeric form.

Reduction of **2** in CH_3CN in the presence of CO leads predominantly to the formation of **2D** together with additional species with ν(CO) bands at 1972, 1940, 1917, and 1726 cm^{-1} (Figure 4a). This latter set of bands is unaffected by reoxidation of **2D** (at −0.9 V; Figure 4b), and the band profile is revealed to match closely that of **1B** (Figure 2) and is attributed to species **2B**. Additional growth features at 1955 and 1918 cm^{-1} are evident in the spectrum, and these indicate the formation of a new species, designated as **2F**. Cycling the potential between −0.9 and −1.4 V results in an increase in the concentrations of **2B** and **2F**, as shown by a comparison of the spectra taken following the first and second reduction/oxidation cycles on the same thin-layer solution (Figure 4c). Oxidation at more positive potentials (0.2 V) results in the substantial recovery (ca. 90%) of **2** (Figure 4d).

Whereas the reduction chemistry of **1** is similar in both CH_3CN and THF,[8] reduction of **2** in THF yields a markedly different product distribution than that found in CH_3CN (Figure S1 of the Supporting Information). The initial reduction of **2** at −1.4 V in THF results in the formation of species that give rise to a complex set of ν(CO) bands between 2022 and 1830 cm^{-1}, as well as several bands in the bridging ν(CO) region. The potential dependence of the spectral changes bears a close similarity to those obtained for **1** where analysis of the spectra reveals the formation of a mixture of **2A**, **2B**, **2C**, and **2D**. The similarity of the reduction chemistry of **1** and **2** is more striking for THF solutions saturated with CO (Figure S2 of the Supporting Information). In this case, the spectra are initially dominated by **2A** (1−5 s) before giving way to **2B**. When the experiment is repeated in the presence of a trace amount of H_2O, the lifetime of **2A** is reduced significantly and **2B** is generated in higher yield.

Differences between the chemistry of **1** and **2** are most pronounced in CH_3CN or THF/CH_3CN mixtures. The reduction chemistry of **1** is dominated by the formation of **1B** together with transient concentrations of **1A**. In contrast, **2A** is not observed under similar conditions, and a relatively stable species with an intermediate oxidation state, **2E**, dominates reductions conducted at mild potentials. No

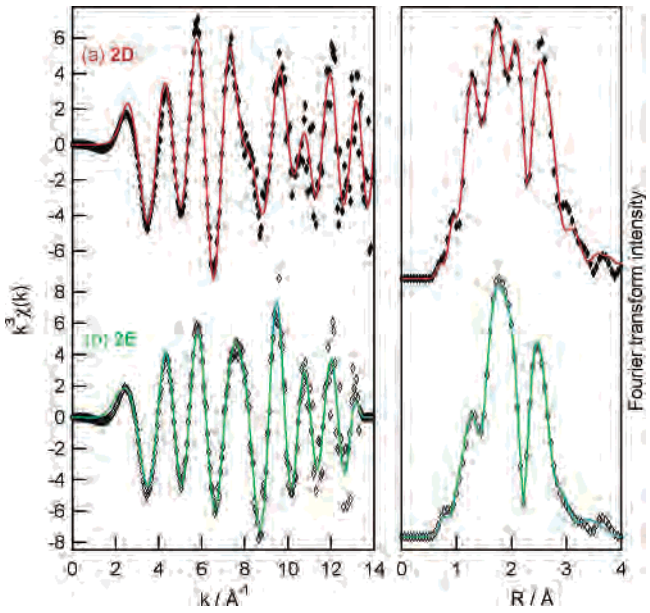

Figure 5. EXAFS and radial distribution functions (without phase correction) of frozen (10 K) CH_3CN solutions of electrochemically generated samples of **2D** and **2E**. The solid line corresponds to the calculated functions.

counterpart of **2E** is observed in the reduction chemistry of **1**. Examination of the potential dependence of the interconversion between **2**, **2E**, and **2D** for solutions having a range of concentrations (1−10 mM) reveals no significant change in the relative intensities of the component bands. The complex band profile for **2E** suggests a diiron compound either that is in rapid equilibrium with another isomeric form or that it is due to a dimeric (tetrairon) species. Careful control of the potential allows generation of solutions predominantly composed of **2E**, and at room temperature, these solutions give a strong signal with $g = 2.032$ and a weak signal with $g = 1.996$. A more complex spectrum is obtained upon cooling the sample to 100 K.

EXAFS of 2D and 2E

Because crystalline samples of **2D** and **2E** could not be obtained, structural information for these species was obtained by the application of EXAFS techniques. Electrochemically generated CH_3CN solutions of **2D** and **2E** were studied by X-ray fluorescence spectroscopy. In both cases, in-line IR spectroscopic measurements showed that impurities due to CO-containing products were below the 5% level (Figure S3 of the Supporting Information). The EXAFS extracted from these measurements are shown in Figure 5 together with best-fit models of the data. Because the IR spectra of **2D** indicate the presence of a bridging CO group, this feature was included in all models. A good fit of the experimental data could be obtained for models having one or two bridging S atoms or one bridging atom and one terminally bound S atom; however, the small differences in the refinement statistics obtained for the different models are not sufficient to permit unambiguous identification of the structure of **2D** (Table S1 of the Supporting Information). This observation reflects the relative insensitivity of the modeling of the EXAFS data to the populations of the scattering atoms.[36] Despite this limitation, reliable model-independent estimates of the Fe−Fe and Fe−S distances are obtained from the analysis. The Fe−Fe distance of 2.56 Å is indicative of a bonding Fe−Fe interaction, and simple electron-counting rules would suggest that rearrangement follows two-electron reduction. This conclusion is supported by the DFT calculations presented in the following section.

The EXAFS of **2E** is substantially different from that of **2D**, and this provides qualitative support for a more substantial change or elaboration of the core geometry, which may accompany dimer formation. While the EXAFS is well fitted using a simple model having a single Fe−Fe separation ($\chi^2 = 1.59$; $R = 11.07\%$), a significant improvement in the statistics (typically $\chi^2 = 0.69$ and $R = 7.33\%$; Table S2 of the Supporting Information) is obtained by the addition of a second Fe−Fe (Fe−Fe$_b$) separation where the relative populations of the Fe−Fe and Fe−Fe$_b$ are set to 1 and 0.5, as would apply for a dimer with a longer inner Fe−Fe separation. While this elaboration of the model introduces two additional parameters, the refinement is not overdetermined, with the number of independent points ($2\Delta k\Delta r/\pi + 2 \approx 20$)[37] greater than the number of refined parameters (15). Whereas the shorter Fe−Fe distance refines to a value of 2.52(1) Å for a range of starting values, the refinement falls into local minima of the Fe−Fe$_b$ distance. Final values of Fe−Fe$_b$ between 2.78 and 3.97 Å were obtained for refinements with initial distances ranging between 2.8 and 4.0 Å. Owing to the limited extent of the data, it is not feasible to extend the analysis to longer distances. In this case, the improvement in EXAFS refinement statistics supports the presence of shorter and longer Fe−Fe interactions, although the reliability of the determination of the longer distance is poor. This limitation in the analysis may be the result of the quality of the data, but it is noted that a double minimum is obtained in the EXAFS analysis of $[Fe_2(\mu\text{-}PPh_2)_2(CO)_6]^{2-}$, where the Fe−Fe distance is 3.63 Å.[7]

The EXAFS analysis when taken together with the ν(CO) band profile, and its constancy during redox transformations and changes in the solvent mixture and temperature, provides support for the dominant species represented by **2E** having a dimeric structure.

The remaining species identified in the SEC experiments, **2F**, has a broad ill-defined ν(CO) band profile and is formed at longer times at more reducing potentials. Because **2F** is formed as a minor product, it is unsuitable for EXAFS analysis. It is not clear from the results currently at hand whether this species is present in solution or it is deposited on the working electrode.

DFT Analysis of the Reduction Products

Species 1A/2A. Because on a fast time scale reduction of **1** and **2** gives a reversible electrochemical response, the initial

(36) Zhang, H. H.; Hedman, B.; Hodgson, K. O. X-ray absorption spectroscopy and EXAFS analysis: the multiple-scattering method and applications in inorganic and bioinorganic chemistry. In *Inorganic Electronic Structure and Spectroscopy*; Lever, A. B. P., Solomon, E. I., Eds.; Wiley: New York, 1999; Vol. 1, pp 513−554. Rehr, J. J.; Albers, R. C. *Rev. Mod. Phys.* **2000**, *72*, 621−654. Penner-Hahn, J. E. *Compr. Coord. Chem. II* **2004**, *2*, 159−186.
(37) Stern, E. A. *Phys. Rev. B* **1993**, *48*, 9825−9827.

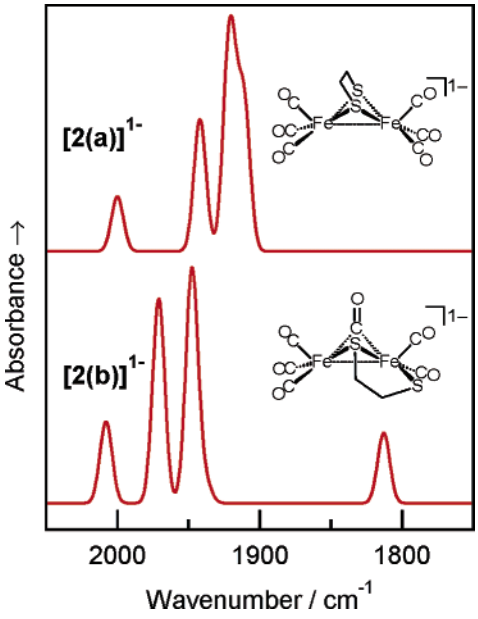

Figure 6. Calculated structures and IR spectra of the one-electron-reduced forms of **2**.

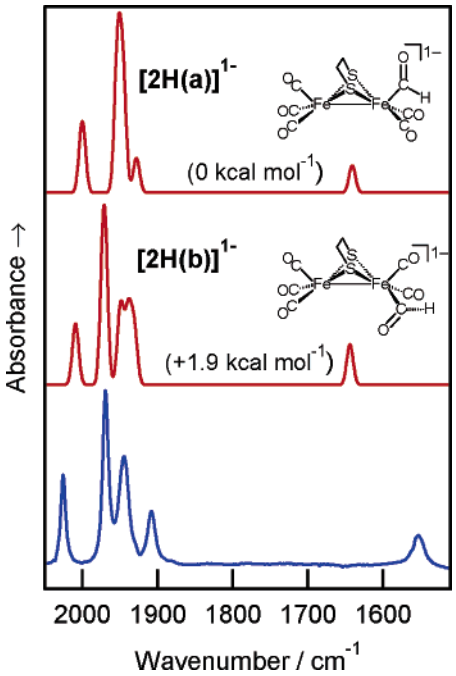

Figure 7. Calculated IR spectra of the apical and basal isomers of the formyl-substituted analogue of **2** and the observed spectrum obtained from the reaction of **2** with $Li[BH(Et)_3]$ in THF. The calculated free energy of the different species relative to **[2H(a)]**$^-$ is given in brackets. To extend the comparison to the seven-CO species, **[2H(h)]**$^-$ (Figure 8), an additional CO molecule is included in the calculation of the free energies.

reduction product may be expected to have a structure similar to that of **2**, i.e., **[2(a)]**$^-$, with two bridging S atoms. A reversible voltammetric response may also be obtained in cases where the reduction products are in equilibrium with a species with a structure closely related to the initial complex provided that the equilibrium is established on a fast time frame relative to diffusion. Accordingly, a species with different binding of the dithiolate bridging ligand without loss or gain of CO ligands, **[2(b)]**$^-$, is also considered.

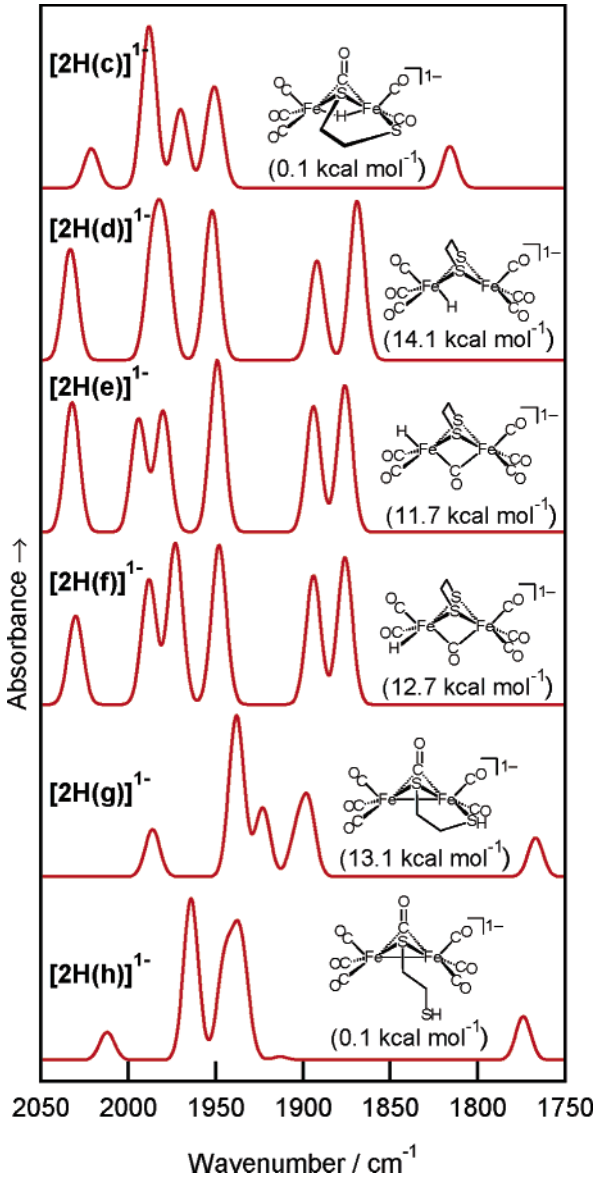

Figure 8. Calculated geometries and IR spectra of the rearrangement products of the formyl derivative of **2**. The calculated free energy of the different species relative to that of **[2H(a)]**$^-$ (structure given in Figure 7) is given in brackets. For **[2H(a**−**g)]**$^-$, an additional molecule of free CO is included in the calculation of the free energies.

The predicted IR spectra of the structural candidates for species **1A**/**2A** are given in Figure 6. In terms of the predicted intensities and ν(CO) values, the simulated IR spectrum of the simple one-electron-reduced species, **[2(a)]**$^-$, is the better match to the experimentally determined spectrum. For **[2(b)]**$^-$, the predicted ν(CO) bands for the terminal CO ligands are not in the correct range, and their relative intensities do not match the experimentally determined spectrum. In addition, the bridging CO ligand in the structure of **[2(b)]**$^-$ leads to a predicted ν(CO) band at 1813 cm^{-1} that is not observed in the IR spectra of **1A**. Gas-phase calculations indicate that **[2(b)]**$^-$ is 7.8 kcal mol^{-1} less stable than **[2(a)]**$^-$.

Species 1B/2B. It has previously been shown that **1B** is readily formed by the reaction of **1** with a hydride source, where the initial formation of a formyl product is supported by IR spectroscopy.[8] In addition to the IR spectra of **1B** and

2B, EXAFS experiments have allowed the determination of the Fe−Fe distance for **1B**. While a DFT analysis has shown that the proposed structure is consistent with the EXAFS and IR spectra,[24] no comparative calculations of the possible alternative structures for **1B** have been reported, nor have there been calculations of the ethanedithiolate-bridged compounds.

Eight possible products resulting from the formal addition of two electrons and one proton to complex **2** are given in Figures 7 and 8. The lowest energy form has a structure with an apical formyl group, **[2H(a)]**$^-$. However, solvation can have an effect on the relative energies of the different species; in the gas phase, **[2H(a)]**$^-$ is calculated to be 1.9 kcal mol^{-1} more stable than the isomer with the formyl group in the basal position, **[2H(b)]**$^-$, but **[2H(a)]**$^-$ is calculated to be 0.4 kcal mol^{-1} *less* stable than **[2H(b)]**$^-$ when solvation by THF is included. The calculated free energies of the different species in the gas phase and with THF and CH_3CN as the solvent are given in Table S3 of the Supporting Information. The experimentally determined IR spectrum in the terminal ν(CO) region of the formyl adduct of **2** is in good agreement with that calculated for **[2H(b)]**$^-$ (Figure 7). The poorer agreement between the observed and calculated wavenumbers of the ν(CO) band of the formyl group in this instance and of the bridging CO group in later examples is partly due to the sensitivity of the mode to interactions with the solvent and partly due to the difficulty in predicting ν(CO) bands for low-energy stretching frequencies.

Experimentally, the formyl derivative of **1** is short-lived, with the stable product of the reaction between hydride and **1** being **1B**.[8] Rearrangement of the formyl derivative of **2** may result in either metal hydrides (**[2H(c−f)]**$^-$) or S-protonated products (**[2H(g,h)]**$^-$), where the DFT-optimized geometries and IR spectra of the different representative structural candidates are given in Figure 8. The highly unfavorable free energies calculated for all of the structures having a terminally bound hydride are evident for both gas-phase and solvated (THF and CH_3CN) species and suggest that these forms do not play a significant role in the reduction chemistry of **2**. While the distinction is less clear for the CH_3CN solvated species, where the difference in calculated free energies is reduced by a factor of 2, a comparison of the free energies of **[2H(c)]**$^-$ and **[2H(g)]**$^-$ suggests that the Fe−Fe bond is more basic than the terminally bound thiolate and is therefore the more likely site of protonation. The seven-CO species **[2H(h)]**$^-$ has approximately the same free energy as the formyl species + CO, although in solution the equilibrium strongly favors the formation of **1B**.[8] In terms of the predicted intensities and ν(CO) values, the simulated IR spectrum of the seven-CO species, **[2H(h)]**$^-$, is the best match to the experimentally determined spectrum. For the rearranged, bridging hydride complex **[2H(c)]**$^-$, the predicted ν(CO) bands for the terminal CO ligands are generally in the correct range. It is clear from the calculated spectra that a terminally bound hydride (**[2H(d−f)]**$^-$) alters significantly the electron richness of the two Fe atoms, giving terminal ν(CO) bands covering a much broader spread of wavenumbers than that observed for **1B**/**2B** (compare Figures 2 and 8).

Table 1. Computed NMR Shielding Tensors and Chemical Shifts for Hydride Ligands

complex	shielding tensor	calcd chemical shift (ppm[a])	exptl chemical shift (ppm)
$[HFe(CO)_4]^-$	39.7219	−8.81[b]	−8.81[c]
$(H)_2Fe(CO)_4$	40.3400	−9.43	−9.67[c]
$[(\mu^2\text{-H})(\mu^3\text{-S})[Fe(CO)_3]_3]^-$	57.8908	−26.98	−23.1[d]
$(\mu^2\text{-H})_2(\mu^3\text{-S})[Fe(CO)_3]_3$	57.9377	−27.03	−24.6[d]
[2H(a)]$^-$	16.2724	+14.64	n/a
[2H(b)]$^-$	18.3941	+12.52	n/a
[2H(c)]$^-$	39.5037	−8.59	n/a
[2H(d)]$^-$	31.3815	−0.47	n/a
[2H(e)]$^-$	36.8830	−5.97	n/a
[2H(f)]$^-$	44.7836	−13.87	n/a
species 1B (minor)	n/a	n/a	−8.94[e]

[a] Relative to TMS. [b] Chemical shift of $[HFe(CO)_4]^-$ set equal to the experimentally determined value of −8.81 ppm relative to TMS. [c] From ref 33. [d] From ref 34. [e] From ref 8.

While the low stability of **2B** has prevented examination of its reaction chemistry, **1B** is reported to react with electrophiles such as CCl_4, PhCOCl, or H^+ to yield $CHCl_3$, PhCHO, and H_2, respectively, together with recovery of **1**.[8] These reactions contrast with the absence of similar chemistry for the close structural analogue $[HNEt_3][(\mu\text{-CO})(\mu\text{-}(2,4,6\text{-trimethylphenyl})S)[Fe(CO)_3]_2]$, studied by Seyferth and coworkers.[38] It was speculated that the difference in chemistry results from the rearrangement of **1B** to a form such as **[2H(e)]**$^-$.[8] The calculated energies of the alternate species (Figure 8) suggest that **[2H(c)]**$^-$ is a far more likely candidate as the hydride donor. The NMR shielding tensors computed for **[2H(a−f)]**$^-$ give predicted values of the chemical shift between −14 and 15 ppm (Table 1). The computed chemical shift of complex **[2H(c)]**$^-$ is an excellent match of the minor resonance observed at −8.84 ppm in the ^{1}H NMR of species **1B**.[8] It is noted that the slow reaction of **1B** may be explained in terms of a slowly established equilibrium with a reactive hydride donor or a quickly established equilibrium with an unreactive hydride donor. Recently, Rauchfuss and coworkers reported that the isomers $(\mu\text{-H})(\mu\text{-edt})[Fe_2(CO)_2(PMe_3)_4]^+$ and $(\mu\text{-CO})(\mu\text{-edt})[Fe_2(CO)H(PMe_3)_4]^+$ exhibit markedly different reactivity as hydride donors, with the bridged hydride being relatively inert.[39] The NMR spectroscopy and low hydride donor reactivity are consistent with **1B**, consisting of an equilibrium mixture of **[2H(h)]**$^-$ as the major form and with the minor species corresponding to the rearranged bridging hydride complex **[2H(c)]**$^-$.

Species 1C/2C. The proposed structure for the "C" type species involves a "B" type fragment, with the pendant thiolate replacing the CO ligand of the neutral parent molecule (Figure 2).[8] The ready conversion of **1C** into **1B** for solutions saturated with CO and recovery of the starting material following oxidation of the "C" type species is consistent with the formulation of the compound. Because the ethylene or propylene linkers do not facilitate electronic communication between the diiron centers, the resulting

(38) Seyferth, D.; Womack, G. B.; Archer, C. M.; Dewan, J. C. *Organometallics* **1989**, *8*, 430−442.
(39) van der Vlugt, J. I.; Rauchfuss, T. B.; Whaley, C. M.; Wilson, S. R. *J. Am. Chem. Soc.* **2005**, *127*, 16012−16013.

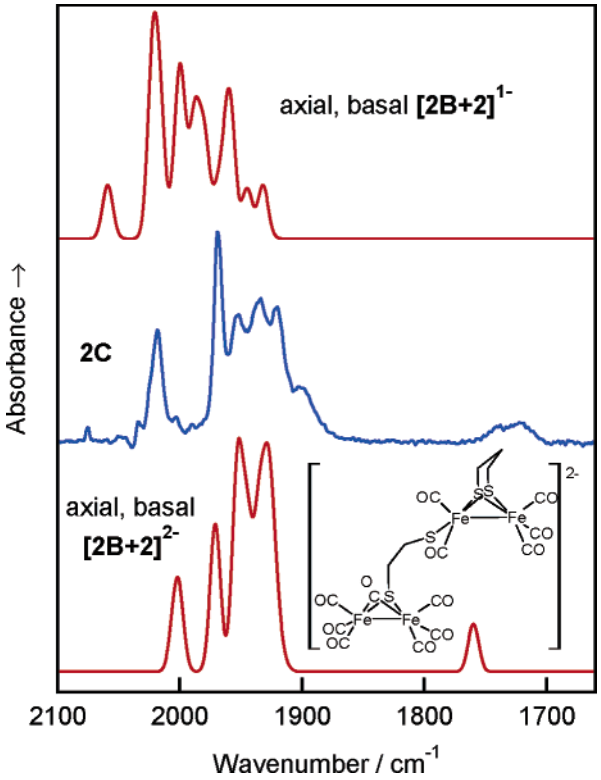

Figure 9. Calculated spectra of the axial,basal isomer of the reduced forms of **[2B+2]** and of a THF solution of **2C**.

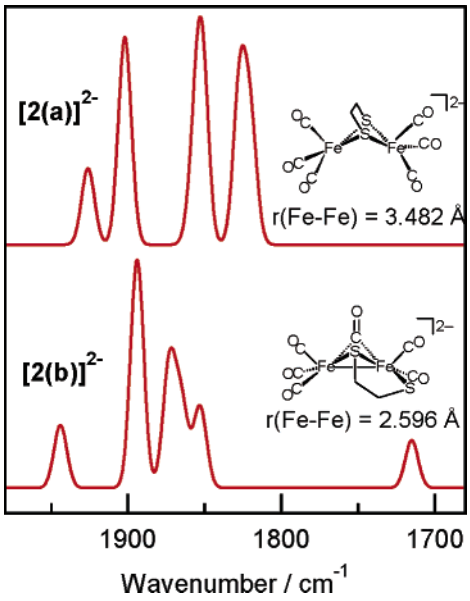

Figure 10. Calculated structures, Fe−Fe separations, and IR spectra of the two-electron-reduced forms of **2**.

spectrum is expected to be little modified from the sum of the parts. For the "B" fragment, the axial and equatorial isomers are possible, and for the 2Fe3S fragment, the terminal thiolate may occupy apical or basal coordination sites. DFT structure optimization based on each of the combinations of isomers of **2C**, $[\mathbf{2B+2}]^{2-}$, proceeds to well-defined minima. The monoanionic forms $[\mathbf{2B+2}]^{-}$ optimize to give structures having only terminally bound CO groups, whereas dianionic $[\mathbf{2B+2}]^{2-}$ retains the bridging CO group in the "B" fragment of the structure. The axial, basal isomer

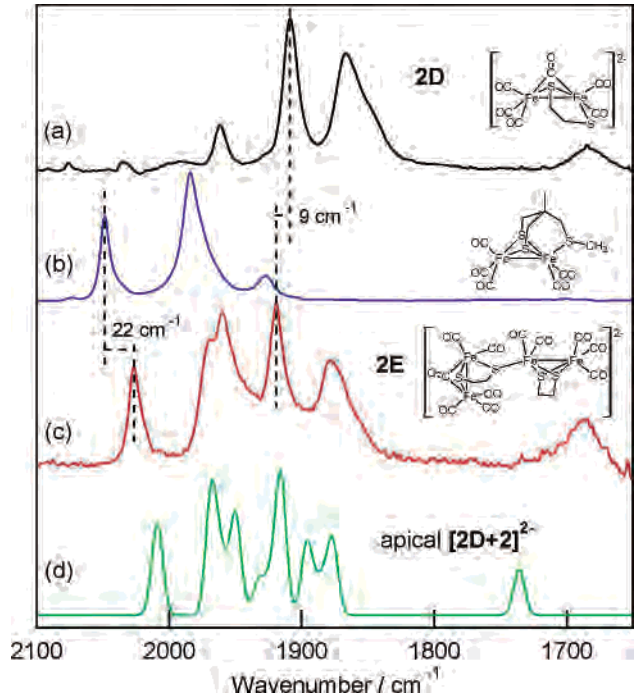

Figure 11. IR spectra of (a) **2D**, (b) $Fe_2(MeC(CH_2S)_3CH_2SMe)(CO)_5$, and (c) **2E** and (d) the calculated IR spectrum of the apical isomer of $[\mathbf{2D+2}]^{2-}$.

of the reduced forms of **[2B+2]** has a terminal ν(CO) band profile in closest agreement with that obtained for **2C** (Figure 9).

Species 1D/2D. The two-electron-reduced species **2D** has a distinct IR spectrum that features a low-wavenumber ν-(CO) band attributed to a bridging CO group. Two starting structures were considered in DFT-based structure optimization, one having two bridging S atoms and the other having one bridging S atom and another terminally bound to one of the Fe atoms. The resulting optimized structures, $[\mathbf{2(a)}]^{2-}$ and $[\mathbf{2(b)}]^{2-}$, differ in terms of the Fe−Fe bonding interaction and the presence of a bridging CO group (Figure 10). In the gas phase, the rearranged product, $[\mathbf{2(b)}]^{2-}$, is computed to be 3.3 kcal mol^{-1} more stable than $[\mathbf{2(a)}]^{2-}$. In addition to presenting a low-wavenumber ν(CO) mode due to the bridging CO group, the IR bands due to terminally bound CO are in closer agreement with the experiment for $[\mathbf{2(b)}]^{2-}$ than $[\mathbf{2(a)}]^{2-}$ (Figure 10). The model-independent value of the Fe−Fe distance obtained from EXAFS analysis of solutions of **2D** in CH_3CN (2.56 Å) matches closely that calculated for $[\mathbf{2(b)}]^{2-}$. Moreover, the analysis of the EXAFS of **2D** is well modeled by the backscattering interactions required for $[\mathbf{2(b)}]^{2-}$ (Figure 5). While the IR spectra, EXAFS and DFT calculations fully support the assignment of the structure of **2D** to $[\mathbf{2(b)}]^{2-}$, the core geometry is relatively uncommon. A similar geometry has been proposed for $(\mu\text{-}PPh_2)(\mu\text{-}CO)[Fe(CO)_3][Fe(CO)_2(PHPh_2)]$ based on NMR and IR spectroscopy,[40] and we are aware of only one other crystallographically characterized bimetallic compound

(40) Yu, Y. F.; Gallucci, J.; Wojcicki, A. *J. Am. Chem. Soc.* **1983**, *105*, 4826−4828.

Scheme 1. Summary of the Reduction Chemistry of **2** in CH_3CN[a]

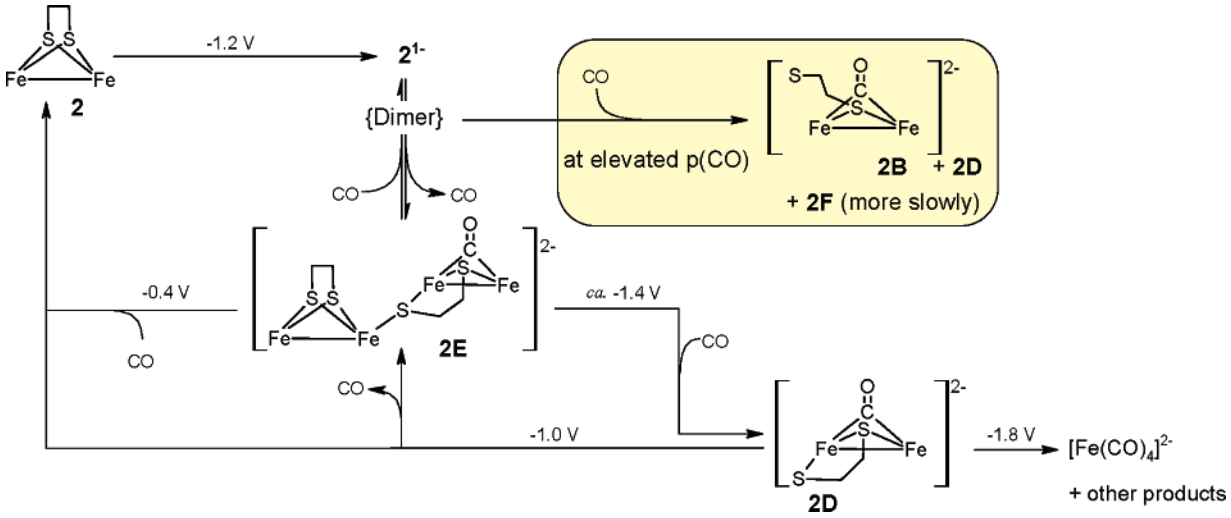

[a] For clarity, the terminally bound CO groups have been omitted from the structures.

with an analogous core geometry, $Ir_2(\mu\text{-S-}t\text{-Bu})(\mu\text{-CO})(CO)_2(\text{S-}t\text{-Bu})(PMe_3)_3$.[41]

Species 2E. The complicated ν(CO) spectrum obtained for **2E** has a group of bands with a profile closely matching that of **2D** but shifted to higher energy by 9 cm^{-1} (Figure 11). The magnitude of the shift is much smaller than that expected for a change in the redox state for the diiron fragment. This expectation is supported by DFT calculations of **[2(b)]**$^-$, where the average shift of the terminal ν(CO) bands is ca. 75 cm^{-1}. Elaboration of **[2(b)]**$^{2-}$ by the donation of an electron pair by the terminally bound S atom to a second diiron fragment would account for the small shift of the ν(CO) bands while retaining the general band profile. The remaining high-wavenumber component of **2E** has a band profile nearly identical with that of the 2Fe3S compounds $Fe_2(MeC(CH_2S)_3CH_2SR)(CO)_5$, R = Me or Ph (Figure 11), and Fe_4S_4L, although differing in energy by 22 and 9 cm^{-1}, respectively.[10,42] While presenting difficulties with the interpretation of the EPR spectrum, the IR spectra suggest a **2D** fragment linked by the terminal S ligand to a decarbonylated form of **2**. The prominence of **2E** among the reduction products is markedly higher when CH_3CN is present, and this may be accounted for by CO/CH_3CN substitution or a lowering of the barrier to the formation of the decarbonylated fragment. The formulation of **2E** suggests the latter alternative.

The dimeric structure proposed for **2E**, **[2D+2]**$^{2-}$, has two isomeric forms differing in terms of the stereochemistry of the 2Fe3S unit. DFT structure optimization proceeds to well-defined minima for both the apical and basal isomers, and the calculated IR spectrum of the apical isomer is in good agreement with that observed (Figure 11). Moreover, the shorter Fe−Fe distance obtained from the analysis of the EXAFS of **2E** is in good agreement with the calculated value, and a similar offset between the calculated and EXAFS-derived Fe−S(bridge) distance (0.1 Å) is obtained for **2E**/**[2(b)]**$^{2-}$ and **2E**/**[2D+2]**$^{2-}$. However, the EPR spectrum obtained for **2E** appears to be at odds with the proposed structure because this gives an 18-electron count for each of the Fe atoms. DFT optimization of **[2D+2]**$^{2-}$ with a triplet ground state gives a final structure only ca. 1 kcal mol^{-1} higher in energy than that for the singlet ground state, although for the triplet, the dimer dissociates. Equilibrium between **2E** and species obtained by homolytic cleavage of the Fe−S bond may provide an explanation for the two EPR signals obtained at room temperature; however, further work is needed to resolve this aspect of the spectroscopy.

Conclusions

Despite the apparent simplicity of the voltammetry, the reduction chemistry of **1** and **2** is remarkably complex. The main features of this chemistry have been elucidated by a combination of spectroscopic and computational (DFT) techniques, and for **2**, these are summarized in Scheme 1. It is important to note that validation of the DFT calculations is based on a comparison of structural and spectroscopic evidence, although in the case of the reduced species, the EXAFS-based structural data are limited to the Fe−Fe and Fe−S contacts. Both for **1** and **2**, the course of the reduction chemistry depends on the fate of the one-electron-reduced product. Relative to their respective dimeric forms, **1**$^-$ and **2**$^-$ are unstable, where CO transfer between the diiron centers leads to **1C** and CO loss gives **2E**. Both forms can best be described as linked Fe^IFe^I and Fe^0Fe^0 centers, where the interaction between the diiron centers is greater for **2E** than **1C**. The marked difference in the prominence of the "**D**" and, by implication, "**E**" species for **1** and **2** may be rationalized in terms of the calculated free energies. Rearrangement of **2**$^{2-}$ to **2D** is calculated to be favorable by 8.4 kcal mol^{-1} (CH_3CN), whereas the corresponding rearrangement for **1** is unfavorable by ca. 4 kcal mol^{-1}. The tendency of **1**$^-$ to form **1C** and then the catalytically unreactive species, **1B**, accounts for inhibition of electrocatalytic proton reduc-

(41) Kalck, P.; Bonnet, J. J.; Poilblanc, R. *J. Am. Chem. Soc.* **1982**, *104*, 3069−3077.
(42) Razavet, M.; Davies, S. C.; Hughes, D. L.; Barclay, J. E.; Evans, D. J.; Fairhurst, S. A.; Liu, X.; Pickett, C. J. *Dalton Trans.* **2003**, 586−595.

tion by **1**.[8] For **2**, the reaction path is tipped more in favor of **2E**, with **2B** formed only under more forcing conditions. Accordingly, electrocatalytic proton reduction by **2** is not inhibited by CO.

The SEC results show clearly that the two-electron-reduced products **2D** and **2B** are readily formed at potentials close to that of the primary reduction process. In CH_3CN, **2D** is the dominant species at potentials more negative than −1.65 V, and further reduction of this species leads to decomposition with the formation of $[Fe(CO)_4]^{2-}$. While the primary reduction process involves one-electron reduction of **2**, this is followed by a CE process resulting in the formation of two-electron products. The absence of a distinct wave in the cyclic voltammetry for the following reduction is associated with the rates of the reaction and diffusion processes. The involvement of additional redox processes is consistent with the observation that the diffusion current following the primary reduction waves of **1** and **2** is noticeably higher than that in the case of $(\mu\text{-SEt})_2[Fe(CO)_3]_2$ when recorded under the same conditions.[6] Clearly, the previous assignment[6] of the second distinct reduction wave (with $E_{pc} = -1.86$) in the electrochemistry of **2** to the reduction of **2** is not supported by the current investigation. For these systems, interpretation of the coulometric results can be complicated by dimer formation, leading to apparent stabilization of the one-electron-reduced product.

While the tendency of the H-cluster model compounds to undergo dimerization following one-electron redox reactions from their electron-precise (18-electron) forms clearly has no parallel in the chemistry of the enzyme, these issues will be central to the design of biomimetic catalysts. The reactivity of the reduced species and the sensitivity of the chemistry to small changes of the structure are central to the catalytic activity. The combined spectroscopic, electrochemical, and theoretical approach developed in this study plays a key role in revealing the details of the chemistry redox-activated compounds.

Acknowledgment. S.P.B. gratefully acknowledges the Australian Research Council for funding this research. S.J.B. acknowledges the receipt of an Australian Postgraduate Research Award. The XAFS experiments were performed at the Australian National Beamline Facility with support from the Australian Synchrotron Research Program, which is funded by the Commonwealth of Australia under the Major National Research Facilities Program. We thank Mark I. Bondin and Dr. Garry Foran for expert assistance with the EXAFS experiments and Professors C. J. Pickett and M. Y. Darensbourg for their insights into this chemistry and for encouragement in the development of the work. M.B.H. acknowledges financial support from the National Science Foundation (Grant CHE-0518047) and the R. A. Welch Foundation (Grant A-0648) and thank the Supercomputing Facility, the Tensor Beowulf cluster (Grant NSF MRI-0216275), and the Laboratory for Molecular Simulation at Texas A&M University for computer time and software.

Supporting Information Available: SEC results for **2** in THF under Ar and CO, IR of samples examined by EXAFS, EPR of **2E** at room temperature and 100 K, EXAFS refinement details for **2D** and **2E**, and DFT-computed free energies, IR spectra, and optimized structures. This material is available free of charge via the Internet at http://pubs.acs.org.

IC061211T